Power Electronic Systems
Laboratory

IEEE Transactions on Industrial Electronics, Vol. 59, No. 3, pp. 1376-1388, March 2012.

Bearingless 300-W PMSM for Bioreactor Mixing

T. Reichert
T. Nussbaumer
J. W. Kolar

Eidgenössische Technische Hochschule Zürich
Swiss Federal Institute of Technology Zurich

Bearingless 300-W PMSM for Bioreactor Mixing

Thomas Reichert, *Student Member, IEEE*, Thomas Nussbaumer, *Member, IEEE*, and Johann W. Kolar, *Fellow, IEEE*

***Abstract*—This paper presents a novel exterior rotor topology of a bearingless brushless synchronous motor with rated power of 300 W. Owing to the large possible magnetic gap and the absence of mechanical bearings, this motor is especially qualified for high-purity and low-shear applications (e.g., bioreactor mixing). Both torque and magnetic bearing forces are created inside this disk-shaped motor using a sophisticated control (proportional-integral-differential vector control) with superimposed drive and bearing currents fed to the concentrated combined stator coils. Optimal design is derived based on an electromagnetic analysis using the three-dimensional finite element method (3D-FEM), and the simulation results are verified with a prototype mixer setup.**

***Index Terms*—Bearingless motor, bioreactor stirrer, brushless motor, exterior rotor, self-bearing motor.**

I. Introduction

STIRRED vessel [1]–[4] is the most commonly used type of bioreactor. To grow cell cultures or to conduct similar biological reactions, a uniform and cell-friendly environment has to be provided inside the reactor. Therefore, one or several agitators need to create a loop flow inside the vessel to distribute cell nutrition and air bubbles in a homogeneous manner. These agitators need to provide high torque at usually moderate rotation speeds [2], [5]. The trend in reactor design is toward bottom-mounted agitators, in contrast to mounting from the tank top, because the available space in the tank cap is limited due to inlets for nutrition or air and openings for sensors (e.g., sensors for temperature or pH-value measurements). Moreover, top mounting requires a large head space above the reactor for assembling and disassembling work regarding the mixer head. In this paper, the focus lies on a single bottom-mounted agitator.

For state-of-the-art bioreactors, the rotation energy is transmitted from a motor, which is placed outside of the tank, to the impeller inside the tank by means of magnetic coupling or with a connecting shaft that passes through a sealed hole in the tank. In the case of magnetic coupling, an additional mechanical bearing is needed inside the tank to stabilize the impeller. This bearing suffers from wear, which impacts the mixer purity. Moreover, pinchoff areas are created with the bearing that can harm the cell cultures, which leads to increased cell destruction. In a similar way, the construction type with a shaft and a seal suffers from these two disadvantages. The seal impacts the purity and creates pinchoff areas as well.

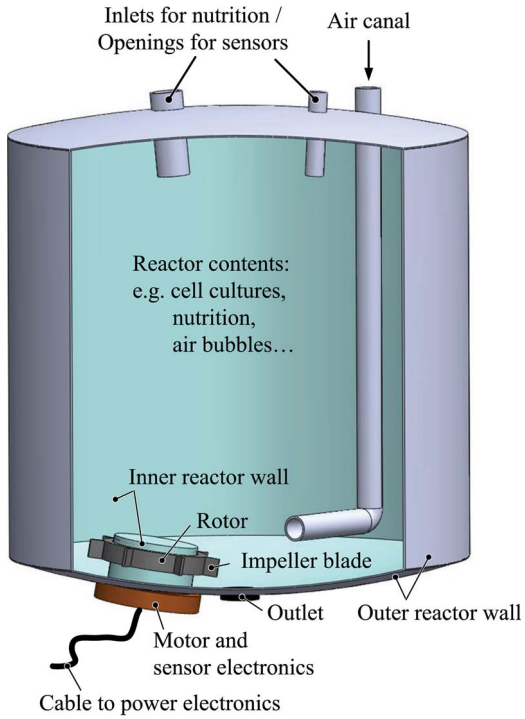

Fig. 1. Sectional view of a stirred bioreactor with a bearingless agitator. For the installation of the motor, an indentation in the tank bottom is needed. This way, only the rotor with impeller needs to be placed inside the reactor.

By employing the bearingless slice motor [6]–[8] as a bioreactor stirrer, the aforementioned disadvantages can be overcome. With this motor technology, which integrates a brushless drive and a magnetic bearing into a single electromagnetic device, a high-purity and low-shear agitator can be built. The bearingless motor requires no shaft and no additional mechanical bearings and has no direct contact with the reactor wall (cf. Fig. 1). Therefore, long life time and low maintenance costs can be guaranteed, since this concept does not suffer from wear and is completely free of lubrication. Moreover, the large possible gap between the rotor and the tank wall makes this motor suitable for clean-in-place and sterilization-in-place applications [9].

For stirring applications, the impeller blades will be mounted onto the rotor, which consists of iron and permanent magnets. Together, this builds the mixer head, which is the only part of the motor that will be placed inside the reactor. The stator with the coils, sensors, and power and sensor electronics will all be placed outside of the tank. Both torque and bearing forces are then transmitted through the tank wall without any mechanical contact. From a process point of view, only small changes are required to integrate the bearingless motor into a

Manuscript received May 31, 2010; revised October 18, 2010; accepted February 14, 2011. Date of publication March 10, 2011; date of current version October 25, 2011.

T. Reichert is with the Power Electronics Systems Laboratory, ETH Zurich, LEM-AMT, 8005 Zurich, Switzerland (e-mail: reichert@lem.ee.ethz.ch).

T. Nussbaumer is with Levitronix GmbH, 8005 Zurich, Switzerland (e-mail: nussbaumer@levitronix.com).

J. W. Kolar is with the Power Electronics Systems Laboratory, ETH Zurich, 8092 Zurich, Switzerland (e-mail: kolar@lem.ee.ethz.ch).

Color versions of one or more of the figures in this paper are available online at http://ieeexplore.ieee.org.

Digital Object Identifier 10.1109/TIE.2011.2126532

bioreactor. An indentation in the tank bottom needs to be added (cf. Fig. 1), but thanks to the large possible magnetic gap, a flexible design is possible, which aims at avoiding any kind of sharp edges. In comparison with a magnetically coupled stirrer, no significant changes in terms of magnetic fields affecting the biological solution will occur. Therefore, considering all the aforementioned reasons, a promising process improvement with higher reaction output can be expected by employing a bearingless motor.

The bearingless motor technology has already proven its advantageous employment in other technological sectors. In the semiconductor industry, canned motor pumps are realized using a bearingless motor, where they help fulfill the strict purity requirements and allow the transport of delicate chemicals [10]–[13]. Moreover, wafer handling devices can be built based on the bearingless technology [14], [15]. In the medical sector, the bearingless motor has been successfully implemented for blood pumps [16], [17], which can be used either externally or, as so-called left ventricular assist devices, implanted into patients to support the heart function. Other possible applications in different industrial sectors (e.g., space, energy sector) include high-speed applications, energy storage in flywheels, and precise angular positioning [18]–[21]. In the majority of these applications, an interior rotor construction is used.

The goal of this paper is to apply the technology of the bearingless motor into the field of bioreactor stirring. For that purpose, a novel bearingless motor using concentrated combined windings will be investigated. In contrary to other bearingless motors with combined windings [14], [22], the focus lies on a setup with exterior rotor construction while employing a new slot/pole ratio.

For a targeted bioreactor with a volume range of 100–300 l, a single bottom-mounted agitator based on the concept of the bearingless slice motor will be developed. The maximum required angular speed is 50 rad/s, which is close to 500 r/min, and the nominal torque is 6 Nm. Thus, the motor has to deliver a nominal power of 300 W.

In Section II, different feasible motor topologies are evaluated, and a choice for a qualified construction is made. The generation of torque and magnetic bearing forces will then be explained in Section III in great detail, and the control implementation is presented in Section IV. Section V shows the results of a design optimization procedure using 3D-FEM analysis, and in Section VI, a thermal analysis is undertaken. Finally, a real-size prototype, based on the optimal design, will be tested in air and in a test water tank to verify the feasibility and the predicted performance measures.

II. Motor Topology

An exterior rotor construction has been chosen, wherefore an indentation in the tank wall is needed (cf. Fig. 1). This construction is advantageous in the case of bottom mounting, because it creates no unwanted flow-low zones, and it does not impact the tank drainage through the main outlet in the middle of the bottom as would be the case for an interior rotor construction, where the rotor would lie inside a bottom extension with the stator placed around it [23]. Moreover, high torque can be provided with an energy-dense exterior rotor construction.

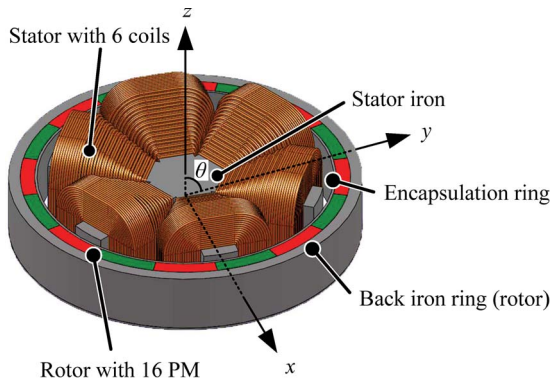

Fig. 2. Computer-aided-design drawing of the proposed motor topology with six stator teeth and a rotor with 16 permanent magnets. The coordinate system indicates the axial (z) and radial (x and y) directions as well as the tilting (with the angle θ).

The optimal impeller diameter for the considered tank volume is in the range of 170 mm. If we consider a 10-mm radial blade length, then a limitation of 150 mm is given for the outer diameter of the rotor. This limited available radial space has to be divided into rotor and stator parts in an optimal ratio to provide the required torque and sufficient bearing forces (cf. Section V). Moreover, there is a magnetic gap of 5 mm between the stator iron and the permanent magnets of the rotor. Considering a setup with stator and rotor encapsulation as well as with the tank wall in between, an actual mechanical fluid gap of 2 mm will result between the tank and the rotor.

In the case of an exterior rotor setup, only a small number of construction possibilities can be considered for the stator, since it has to be placed in the small area within the hollow rotor. Therefore, the available area for the stator, including the windings, is limited so that a tradeoff has to be found between stator iron space and winding space. The torque generation is proportional to the magnetomotive force (measured in ampere turns), which is the product of the winding number and the current through it. Obviously, with respect to a certain maximum allowed current density $J_{\max}$, a higher magnetomotive force can be provided when the space for the coils is enlarged. However, a minimal stator tooth thickness is required to avoid heavy magnetic saturation, which would drastically reduce the torque. Therefore, the number of stator teeth (which is equivalent to the number of stator slots) has to be chosen small. With this measure, the few stator teeth can be designed sufficiently thick while still leaving enough space for the windings around them, which will fill up the slot space (cf. Fig. 2).

The minimal required stator slot number for a functional bearingless motor is 4. With this topology, magnetic bearing forces can be generated independently of the actual rotation angle, but the drive would show disadvantageous single-phase characteristics with rather large cogging torque [23].

A topology with five stator slots results in a five-phase drive with low cogging torque. However, due to the uneven number of stator teeth, there is no magnetic center point for the bearing. This means that high bearing currents are permanently needed to levitate the rotor. As a result, the available power for the drive is limited when the maximum current density $J_{\max}$ is respected.

For a slot number of 6, a promising topology can been found. In combination with a 16-pole rotor, this motor provides a three-phase bearing that levitates the rotor, whereas a three-phase drive control guarantees smooth rotation with almost zero cogging torque.

Motor topologies with stator slot numbers higher than 6 are not considered any more, since the remaining space for windings would be too small to place coils that can provide sufficient magnetomotive force.

Hence, an exterior rotor construction with a slot/pole pair ratio of 6/8 (cf. Fig. 2) has been found to be the optimal choice for the dedicated bioreactor applications. The stator is made of laminated iron and holds one coil on each tooth. The rotor consists of an outer iron ring (back iron) and 16 permanent magnets that are radially magnetized in alternating order. This motor concept with six stator teeth would also work with other rotor pole pair numbers p as long as they fulfill the condition of

$$p = 2 + (n \cdot 6), \quad n = 0, 1, 2, \ldots. \tag{1}$$

If this condition is respected, then the mutual drive torque and the bearing force generation with the same three-phase control concept (cf. Section III) is possible. Therefore, the rotor could alternatively be built with 4 or 28 permanent magnets, but the 3D-FEM simulations (cf. Section V) confirmed that 16 magnets is the optimal choice.

III. Torque and Bearing Forces

To stabilize all six motion degrees of freedom (DOF) of the rotor, the magnetic bearing must cope with radial (2 DOF) and axial (1 DOF) displacements as well as tilting (2 DOF). The remaining DOF is the rotation of the rotor around its main axis, which is controlled by the drive.

All the DOFs of the rotor are affected by attracting reluctance forces that occur between the stator iron and the rotor magnets. In the case of the drive, this can lead to disturbing cogging torque, and it is mandatory to minimize this effect when designing the motor. In the case of the magnetic bearing, these forces have both stabilizing and destabilizing effects, depending on the direction of the rotor displacement. This is in accordance with Earnshaw's theorem [24], from which it can be derived that it is not possible to stabilize all the DOFs of motion solely based on passive forces. Therefore, the magnetic bearing can be split into passive and active parts.

A. Passive Bearing

For the proposed disk-shaped rotor, the aforementioned attracting reluctance forces are already sufficient to stabilize the axial position and the tilting [25]. Whenever the rotor is moved away from its center position, the restoring forces grow linearly (in the small working range) with the displacement (with an axial force displacement factor k_z and a restoring torque factor k_θ dependent on the angular displacement, respectively) and counteract the movement. Thus, the magnetic bearing for three DOFs can be built as a passive bearing if these force displacement factors are sufficiently large, which can be influenced with the motor design.

These three DOFs are not damped actively. Thus, an excitation can lead to a displacement oscillation which would only be damped by the media surrounding the rotor. This could be critical for an application running in air, as the oscillations would only cease slowly, but for the targeted bioreactor application, the process liquid quickly dampens the undesired rotor movement (cf. Section VII).

The attracting reluctance forces influence the radial displacement as well. In this case, however, a dislocation from the center position leads to a resulting reluctance force that supports the movement of the rotor. When the movement starts, the magnetic gap on one side becomes narrower, and the movement will not stop until a mechanical touchdown. Thus, there is no stable radial position when levitating the rotor, and countermeasures by means of an active electromagnetic bearing have to be taken to keep the rotor in the center position. This destabilizing force grows with increasing displacement and can be described by a force displacement factor k_r. Hence, the motor design should aim at keeping this factor small to maintain the required active control forces in a low range. Obviously, the media surrounding the rotor will also dampen the movement in the radial direction.

B. Active Bearing

An active magnetic bearing is necessary to stabilize the two DOFs in the radial direction. For the control, permanent knowledge about the current rotor position (in the x- and y-directions) and about the electrical angle is mandatory. This electrical rotor angle

$$\varphi_{\mathrm{elec}} = p \cdot \varphi_{\mathrm{mech}} \tag{2}$$

which is the product of the pole pair number p and the mechanical rotation angle φ_{mech}, determines the phase of the sinusoidal bearing currents.

For this bearing with six stator coils, three nonadjacent stator teeth together build a three-phase system (e.g., coils 1, 3, and 5) in terms of the applied sinusoidal currents, whereas there is a phase shift of 180° between the currents of two opposite coils (e.g., coils 1 and 4; cf. Fig. 3). With this arrangement, a rotating magnetic field with the mechanical rotation frequency is created. According to the theory of bearingless motors [26], the rotor pole pair number p has to be equal to the harmonic order of the drive, i.e.,

$$\frac{f_{\mathrm{drv}}}{f_{\mathrm{mech}}} = p \tag{3}$$

whereas the relation with the bearing should be

$$\frac{f_{\mathrm{bng}}}{f_{\mathrm{mech}}} = p \pm 1. \tag{4}$$

From this point of view, with respect to (4), a rotor with a pole pair number of 2 has to be chosen. In combination with the harmonics generated by the six slot stator [27], the bearingless motor can be controlled for different rotor pole pair numbers if (1) is respected.

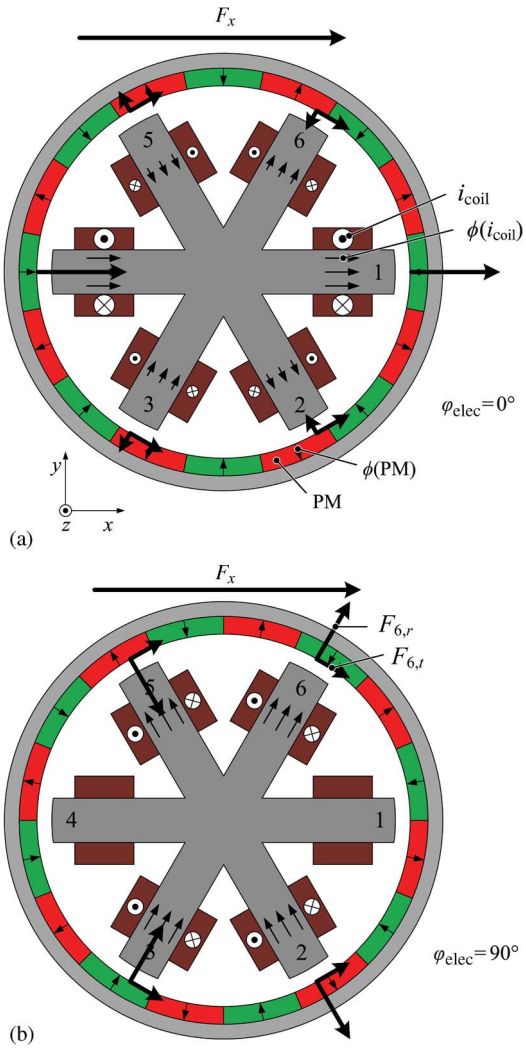

Fig. 3. Radial force generation in the x-direction based on both radial and tangential force generations for two specific rotation angles. (a) $\varphi_{\mathrm{elec}} = 0°$. (b) $\varphi_{\mathrm{elec}} = 90°$. The length of each arrow represents the actual flux or force impact, respectively.

In the control, the radial position in the x- and y-directions is controlled separately. The value of the radial displacement is fed to a PID controller, which then determines the amplitude of the bearing currents. Fig. 3 shows the generation of a force into the positive x-direction. Each coil produces a magnetic flux that interacts with the flux of the permanent magnets. When the rotor turns, the influence of the flux due to the permanent magnets varies in a sinusoidal way as the magnets pass the stator teeth. Both radial (referred to as Maxwell forces) and tangential forces (referred to as Lorentz forces) are created by each coil, and their superposition leads to a force component per coil of

$$F_{n,x}(\varphi_{\mathrm{elec}}) = \cos\left(\varphi_{\mathrm{elec}} + (n-1)\cdot\frac{\pi}{3}\right)\cdot N_{\mathrm{coil}}\cdot\hat{I}_{\mathrm{bng}} \cdot\left[\cos\left((n-1)\cdot\frac{\pi}{3}\right)\cdot\cos\left(\varphi_{\mathrm{elec}}+(n-1)\cdot\frac{2\pi}{3}\right)\cdot k_{I,\mathrm{Fr}} + \sin\left((n-1)\cdot\frac{\pi}{3}\right)\cdot\sin\left(\varphi_{\mathrm{elec}}+(n-1)\cdot\frac{2\pi}{3}\right)\cdot k_{I,\mathrm{Ft}}\right] \quad (5)$$

with the force current factor $k_{I,\mathrm{Fr}}$ in the radial direction, the force current factor $k_{I,\mathrm{Ft}}$ in the tangential direction, the winding number N_{coil}, and the amplitude of the bearing current $\hat{I}_{\mathrm{bng}}$.

Thus, each force component depends on the actual coil current, the actual position of the corresponding stator tooth with respect to the desired force direction, and the actual permanent magnet position in front of the tooth.

The total resulting force is then given by

$$F_x = \sum_{n=1}^{6} F_{n,x} = \left(\frac{3}{2}\cdot k_{I,\mathrm{Fr}} + \frac{3}{2}\cdot k_{I,\mathrm{Ft}}\right)\cdot N_{\mathrm{coil}}\cdot\hat{I}_{\mathrm{bng}} = k_{I,F}\cdot N_{\mathrm{coil}}\cdot\hat{I}_{\mathrm{bng}} \quad (6)$$

where the force current factors $k_{I,\mathrm{Fr}}$ and $k_{I,\mathrm{Ft}}$ can be scaled and summed up to a total force current factor $k_{I,F}$.

The same force calculation can be done in the y-direction, where the partial force per coil becomes

$$F_{n,y}(\varphi_{\mathrm{elec}}) = \sin\left(\varphi_{\mathrm{elec}} + (n-1)\cdot\frac{\pi}{3}\right)\cdot N_{\mathrm{coil}}\cdot\hat{I}_{\mathrm{bng}} \cdot\left[-\sin\left((n-1)\cdot\frac{\pi}{3}\right)\cdot\cos\left(\varphi_{\mathrm{elec}}+(n-1)\cdot\frac{2\pi}{3}\right)\cdot k_{I,\mathrm{Fr}} + \cos\left((n-1)\cdot\frac{\pi}{3}\right)\cdot\sin\left(\varphi_{\mathrm{elec}}+(n-1)\cdot\frac{2\pi}{3}\right)\cdot k_{I,\mathrm{Ft}}\right]. \quad (7)$$

The total resulting force can again be found by superimposing all force components as

$$F_y = \sum_{n=1}^{6} F_{n,y} = \left(\frac{3}{2}\cdot k_{I,\mathrm{Fr}} + \frac{3}{2}\cdot k_{I,\mathrm{Ft}}\right)\cdot N_{\mathrm{coil}}\cdot\hat{I}_{\mathrm{bng}} = k_{I,F}\cdot N_{\mathrm{coil}}\cdot\hat{I}_{\mathrm{bng}}. \quad (8)$$

It can be seen from (6) and (8) that the radial forces in the x- and y-directions can be controlled with the applied bearing currents, and the producible force per current (with factor $k_{I,F}$) is independent of both rotor angle and force direction for this current feed. This is confirmed in Fig. 4, where the single force components are shown dependent on the electrical angle and then summed up to the total force in the x- and y-directions. For the excitation, a three-phase sinusoidal magnetomotive force $(N_{\mathrm{coil}}\cdot\hat{I}_{\mathrm{bng}})$ with a peak value of 1000 At is applied exemplarily.

All the force current factors as well as the force displacement factors mentioned before have actually been linearized around the working point. For example, the attracting Maxwell force would have a quadratic relation with the rotor displacement if only one stator tooth was considered. However, due to the arrangement with six stator teeth (two opposite teeth create counteracting radial forces), a linear force displacement dependence can be observed for a small radial displacement within the working range of 2 mm. This property is promoted by the large magnetic gap and the thick magnets (which in the calculation of the magnetic reluctance have similar properties than the magnetic gap because of their relative permeability close to 1) with respect to the small rotor displacement.

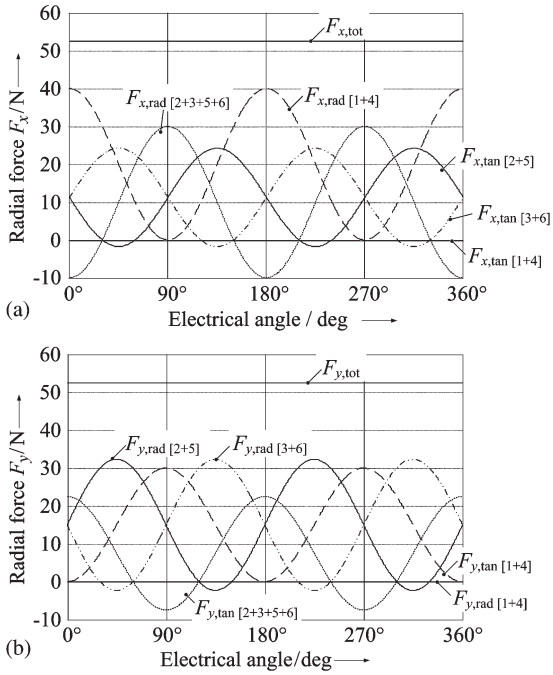

Fig. 4. Radial and tangential force components dependent on the electrical angle for the generation of a constant radial force in the (a) x-direction and (b) y-direction with an applied sinusoidal magnetomotive force (three-phase) with a peak value of 1000 At.

C. Drive Control and Torque Generation

For the control of the drive, another three-phase system has to be implemented. However, only tangential forces are desired, since radial forces cannot contribute to any torque generation and would only disturb the bearing. Similar to the control of the bearing, three nonadjacent coils build one three-phase system. This time, however, the currents in two opposite coils have no phase shift, and both coils contribute to the torque equally. With this arrangement, a rotating magnetic field with twice the mechanical rotation frequency is created. Together with the harmonics generated by the six stator slots [27], (3) is satisfied for the proposed setup, where the pole pair number of the rotor is 8. Thanks to the employed three-phase control, smooth rotation is guaranteed for this drive.

There is no actual torque control but rather a speed control, assuming that the required torque can be provided until the current limit is reached. Thus, the actual speed (as the derivative of the rotor angle) is compared to the reference speed, and the error is fed to a PI controller, which will determine the amplitude of the drive currents.

In Fig. 5, the torque generation is explained using the example of the same two specific rotation angles as for the magnetic bearing. Each coil contributes to the torque with

$$T_n(\varphi_{\mathrm{elec}}) = k_{I,\mathrm{Tn}} \cdot \sin^2\left(\varphi_{\mathrm{elec}} + (n-1)\cdot\frac{2\pi}{3}\right) \cdot N_{\mathrm{coil}} \cdot \hat{I}_{\mathrm{drv}} \tag{9}$$

with the torque current factor $k_{I,\mathrm{Tn}}$ (equal for all coils), the amplitude of the drive current $\hat{I}_{\mathrm{drv}}$, and the winding number N_{coil}, which is the same for both drive and bearing, since there

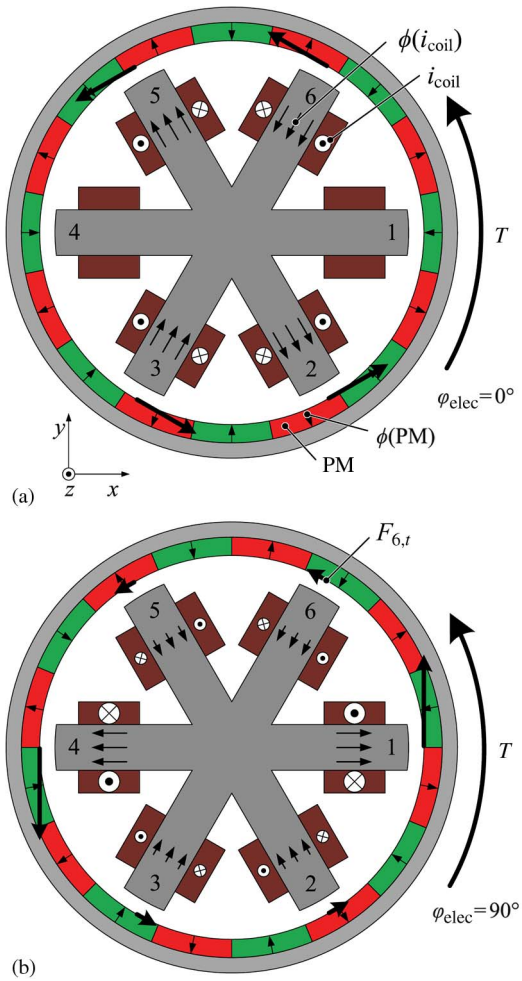

Fig. 5. Torque generation based on tangential force generation for two specific rotation angles. (a) $\varphi_{\mathrm{elec}} = 0°$. (b) $\varphi_{\mathrm{elec}} = 90°$. The length of each arrow represents the actual flux or force impact, respectively.

is only one coil on each stator tooth. Since all the radial forces cancel each other out, they are omitted in the illustration in Fig. 5. The total torque becomes

$$T = \sum_{n=1}^{6} T_n = 3 \cdot k_{I,\mathrm{Tn}} \cdot N_{\mathrm{coil}} \cdot \hat{I}_{\mathrm{drv}} = k_{I,T} \cdot N_{\mathrm{coil}} \cdot \hat{I}_{\mathrm{drv}} \tag{10}$$

with an overall torque current factor $k_{I,T}$.

D. Superposition for Rotor Control

Up to now, the active magnetic bearing and the drive control have been looked at separately, whereas for operation, both control systems need to work simultaneously. This could be achieved by putting two coils onto each stator tooth, one for the bearing and one for the drive, and run the two control systems independently on separate coils. However, there are always at least two stator teeth where the drive and the bearing control generate opposing forces. In this case, the applied currents produce forces that partially cancel each other out. Therefore, concerning the copper losses, it is recommended to use only

one coil per stator tooth and to mathematically superimpose the required control currents already in the control unit [22]. This proposition can be justified if a maximum current density $J_{\max}$ is respected, leading to a maximum magnetomotive force $\Theta_{\max,\mathrm{rms}}$ of

$$\Theta_{\max,\mathrm{rms}} = J_{\max} \cdot A_{\mathrm{coil}} \tag{11}$$

with the available winding area A_{coil}. For a given winding number N_{coil}, the maximum allowed current is then

$$I_{\max,\mathrm{rms}} = \frac{\Theta_{\max,\mathrm{rms}}}{N_{\mathrm{coil}}} = J_{\max} \cdot \frac{A_{\mathrm{coil}}}{N_{\mathrm{coil}}}. \tag{12}$$

In the case of separated windings, the available winding area per tooth has to be split in the design for the drive and the bearing with a factor n between 0 and 1, leading to

$$A_{\mathrm{coil,drv}} = n \cdot A_{\mathrm{coil}} \tag{13}$$

$$A_{\mathrm{coil,bng}} = (1-n) \cdot A_{\mathrm{coil}}. \tag{14}$$

With respect to (11), the maximum magnetomotive forces applicable to the coils become

$$\begin{aligned}\Theta_{\mathrm{drv,max,rms}} &= J_{\max} \cdot n \cdot A_{\mathrm{coil}} \\ &= n \cdot \Theta_{\max,\mathrm{rms}} \end{aligned} \tag{15}$$

$$\begin{aligned}\Theta_{\mathrm{bng,max,rms}} &= J_{\max} \cdot (1-n) \cdot A_{\mathrm{coil}} \\ &= (1-n) \cdot \Theta_{\max,\mathrm{rms}}. \end{aligned} \tag{16}$$

When a maximum current density is respected, the ohmic losses are inversely proportional to the winding area and proportional to the square of the magnetomotive force. In case of separated windings, the losses become

$$\begin{aligned}P_{L,s} &\sim 6 \cdot \frac{(n \cdot \Theta_{\max,\mathrm{rms}})^2}{n \cdot A_{\mathrm{coil}}} + 6 \cdot \frac{((1-n) \cdot \Theta_{\max,\mathrm{rms}})^2}{(1-n) \cdot A_{\mathrm{coil}}} \\ &= 6 \cdot \frac{\Theta^2_{\max,\mathrm{rms}}}{A_{\mathrm{coil}}}. \end{aligned} \tag{17}$$

In the case of combined windings (drive and bearing currents in one coil), the required forces are either added or subtracted (cf. Figs. 3 and 5). Therefore, a summation of the drive and bearing currents will result in three of the six stator coils, whereas a subtraction of the two currents is applied in the case of the remaining three coils. It can be proven that this relationship becomes independent of the phasing between the drive and bearing currents when all six coils are considered together. Hence, the losses for combined windings become

$$\begin{aligned}P_{L,c} &\sim 3 \cdot \frac{(n \cdot \Theta_{\max,\mathrm{rms}} + (1-n) \cdot \Theta_{\max,\mathrm{rms}})^2}{A_{\mathrm{coil}}} \\ &\quad + 3 \cdot \frac{(n \cdot \Theta_{\max,\mathrm{rms}} - (1-n) \cdot \Theta_{\max,\mathrm{rms}})^2}{A_{\mathrm{coil}}} \\ &= 6 \cdot \frac{(2n^2 - 2n + 1) \cdot \Theta^2_{\max,\mathrm{rms}}}{A_{\mathrm{coil}}}. \end{aligned} \tag{18}$$

If the losses of the two arrangements are compared, it results that the losses of the combined winding arrangement are always smaller because of

$$\frac{P_{L,c}}{P_{L,s}} = 2n^2 - 2n + 1 < 1, \quad n \in]0,1[. \tag{19}$$

That is, in the ideal case, if both drive and bearing currents have the same amplitude ($n = 0.5$), the losses can be reduced by a factor of 50% using combined windings. If a motor with separated coils is run in a different operating point than the one it was designed for, then the efficiency difference to a motor with combined windings can become even worse.

IV. Digital Control

Fig. 6 depicts the overall control scheme for the proposed motor topology. It is divided into a mechanical and an electrical system and into digital control. The mechanical system consists of two plants for the drive and for the radial bearing. Whenever the torque output of the electrical system is different from the load torque T_L, the motor is accelerated or decelerated. According to (10), the torque is proportional to the drive current so that the drive can be modeled with

$$T = k_{I,T} \cdot N_{\mathrm{coil}} \cdot \hat{i} - T_L. \tag{20}$$

In the plant of the bearing, the force output of the electrical system is opposed by disturbance forces $\tilde{F}_{x,y}$ (or more generally noted as $\tilde{F}_r$) and by a velocity proportional damping (with factor D) dependent on the mixer surroundings, such as the viscosity of the fluid. Additionally, the bearing is under the influence of destabilizing reluctance forces (with factor k_r). As shown in (6) and (8), the active bearing forces are proportional to the bearing currents, and the bearing can then be modeled with

$$F_r = k_r \cdot r + k_{I,F} \cdot N_{\mathrm{coil}} \cdot \hat{i} - D \cdot \dot{r} - \tilde{F}_r \tag{21}$$

given that there are two star connections (cf. Fig. 7). Since these measured currents are composed of drive and bearing parts, a transformation has to be done first. By adding the currents of two opposite coils, the drive current in that phase can be determined, whereas the bearing currents can be obtained using subtraction. Then, the three-phase currents are transformed into a two-phase rotor-dependent coordinate system (field-oriented control). All these transformations can be summarized into a single matrix $\mathbf{T}$, which depends on the current electrical angle and is given by

$$\mathbf{T} = \begin{pmatrix} c_\varphi - \frac{\sqrt{3}}{3} \cdot s_\varphi & -\frac{2\cdot\sqrt{3}}{3} \cdot s_\varphi & c_\varphi - \frac{\sqrt{3}}{3} \cdot s_\varphi & -\frac{2\cdot\sqrt{3}}{3} \cdot s_\varphi \\ s_\varphi + \frac{\sqrt{3}}{3} \cdot c_\varphi & \frac{2\cdot\sqrt{3}}{3} \cdot c_\varphi & s_\varphi + \frac{\sqrt{3}}{3} \cdot c_\varphi & \frac{2\cdot\sqrt{3}}{3} \cdot c_\varphi \\ c_\varphi + \frac{\sqrt{3}}{3} \cdot s_\varphi & \frac{2\cdot\sqrt{3}}{3} \cdot s_\varphi & -c_\varphi - \frac{\sqrt{3}}{3} \cdot s_\varphi & -\frac{2\cdot\sqrt{3}}{3} \cdot s_\varphi \\ s_\varphi - \frac{\sqrt{3}}{3} \cdot c_\varphi & -\frac{2\cdot\sqrt{3}}{3} \cdot c_\varphi & -s_\varphi + \frac{\sqrt{3}}{3} \cdot c_\varphi & \frac{2\cdot\sqrt{3}}{3} \cdot c_\varphi \end{pmatrix} \tag{22}$$

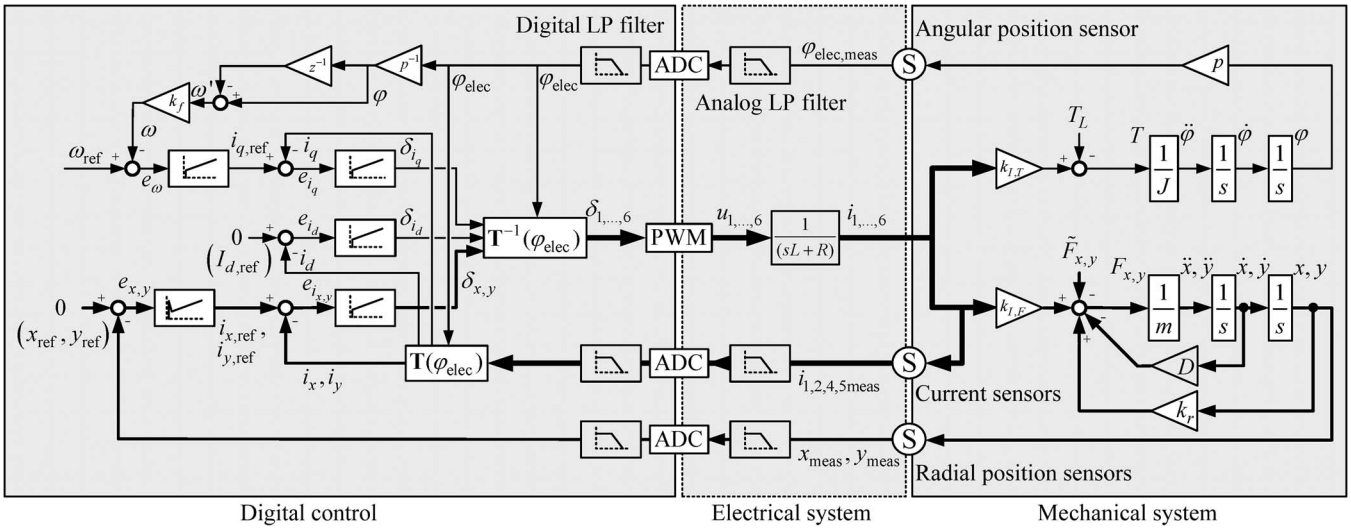

Fig. 6. Control scheme of the bearingless permanent magnet synchronous motor. Drive and bearing are handled separately in the digital control part and are then combined [using the inverse of the transformation function $\mathbf{T}(\varphi_{\mathrm{elec}})$] prior to applying the PWM signals to the six stator coils. In the plant of the radial position control, the destabilizing force displacement factor k_r and velocity proportional damping D are considered.

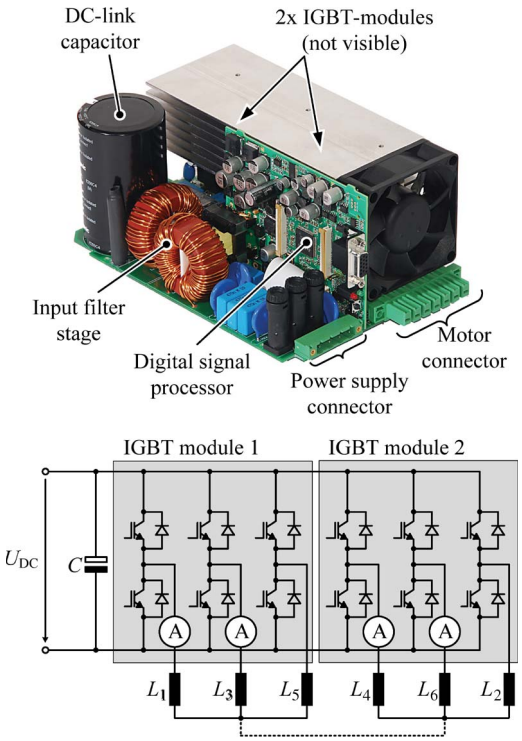

Fig. 7. Picture of the employed power electronics with two integrated IGBT modules. Each module consist of three half bridges that are all fed by the dc link voltage. Each stator coil is connected with one half bridge, and three nonadjacent coils are connected in star. Alternatively, the motor can be run when all the coils are connected with only one star point.

where c_φ stands for $\cos(\varphi_{\mathrm{elec}})$, and s_φ stands for $\sin(\varphi_{\mathrm{elec}})$. The whole transformation can be stated as

$$\begin{pmatrix} i_d \\ i_q \\ i_x \\ i_y \end{pmatrix} = \mathbf{T} \bullet \begin{pmatrix} i_1 \\ i_3 \\ i_4 \\ i_6 \end{pmatrix}. \tag{23}$$

For digital control, permanent knowledge about the angular and radial rotor positions is mandatory. Since the control is built as a cascade with an inner current control loop, knowledge about the coil currents is required as well. Therefore, four of the six coil currents need to be measured constantly with sensors. The remaining two can be calculated. In the control, the radial positions are compared to reference values (usually zero), and the errors are fed to PID controllers according to

$$K_{\mathrm{PID}}(z) = K_P + \frac{K_I}{1 - z^{-1}} + K_D(1 - z^{-1}). \tag{24}$$

The outputs are reference currents, which are compared to the actual bearing currents. This time, the errors are fed to PI controllers according to

$$K_{PI}(z) = K_P + \frac{K_I}{1 - z^{-1}}. \tag{25}$$

Similarly, the actual angular velocity (calculated from the electrical angle in the control) is compared with a reference speed, and the error is fed to a PI controller. The output is a reference drive current for the inner loop, and it is compared to the actual drive current using another PI controller.

The outputs of all the inner control loops are then the duty cycles of the PWM, which need to be transformed back using $\mathbf{T}^{-1}$, prior to applying them to the six stator coils.

Fig. 7 shows the employed power electronics [28]. On the motor side, it consists of two insulated gate bipolar transistor (IGBT) modules that are fed with the dc link voltage. Each module provides three half bridges, and three nonadjacent coils are connected with one end to a half bridge of the same module, whereas the other ends are connected together in star. The motor can alternatively be run with all six stator coils connected in one star point. However, the system is then underdetermined since only four currents are measured with sensors.

Digital control is calculated in the DSP of the power electronics. The TMS320F2811 from Texas Instruments Incorporated

runs with 150 MHz, and it uses fixed-point arithmetic. The control cycles are clocked with 17.5 kHz. All the measured signals (radial position, rotor angle, and coil currents) are first filtered using analog components before they are digitalized using the 12-bit analog digital converter inputs from the DSP. Thereafter, they are digitally filtered as well and then fed to the control algorithms. In the end, the output signals of the digital control are the PWM duty cycles for the IGBTs. These duty cycles have an accuracy of 16 bits with a range limitation from 5% to 95%.

V. Design Optimization

For the design optimization, an extended magnetostatic 3D-FEM simulation has been conducted. The goal is to determine optimal values for the geometric variables so that the motor will provide sufficient torque and bearing forces.

A. Fixed Design Parameters

The values of some design parameters are already given by the application, whereas other variables can be varied to optimize the motor performance. Owing to the targeted tank volume, the outer rotor diameter is fixed to 148 mm, considering a rotor encapsulation of 1-mm thickness. For the maximum current density $J_{\max}$, a value of 5 A/mm^2 has been chosen so that the motor can be run with conventional passive air cooling. Together with the available areal space for the windings A_{coil}, this will determine the maximum allowed magnetomotive force $\Theta_{\max,\text{rms}}$ according to (11) and the maximum coil current according to (12).

B. Optimal Design Variables

The remaining geometric variables (shown in Fig. 8) can be varied. The optimization procedure for such a topology is described in [29] in great detail. In a first step, the optimal radial motor dimensions have to be found. This will then determine the rotor size and the ratio of back iron to magnet thickness as well as the stator size. In a second step, the stator teeth have to be optimized, which is basically a tradeoff between winding and iron space. For the stator teeth, it was found that bar-shaped teeth are recommendable [29]–[31].

This optimization was carried out for setups with rotor pole pair numbers of 2, 8, and 14. With a pole pair number of 2, however, the back iron would have to be rather thick to avoid saturation, and in consequence, the stator would have to be built small. With a pole pair number of 8 or even 14, the overall radial rotor thickness is smaller so that the stator can be built as large as possible. The disadvantage of higher pole pair numbers is the larger rotational frequency of the magnetic fields. Considering the easiness of control as well as the losses (cf. Section VI), it is recommendable to keep the pole pair number low. For all these reasons, the construction with a pole pair number of 8 was found to be optimal. Additionally, the optimization of the stator teeth width revealed that for a rotor with 16 permanent magnets, the width ratio of one magnet with respect to the stator tooth is slightly larger than 1; thus, an ideal flux linkage is created. Hence, there would be no additional benefit if larger magnets (smaller pole pair number) were used. For the stator, the tradeoff between iron and winding space is determined by both passive and active forces. If the stator tooth width is enlarged, it leads to an increase in all the passive forces, since there is a larger flux linkage with the magnets. For the windings, on the other hand, the stator teeth should be small so that large coils can be wound around them. When the maximum current density is respected, the magnetomotive force (hence, the active bearing forces and the torque) linearly depends on the available winding area.

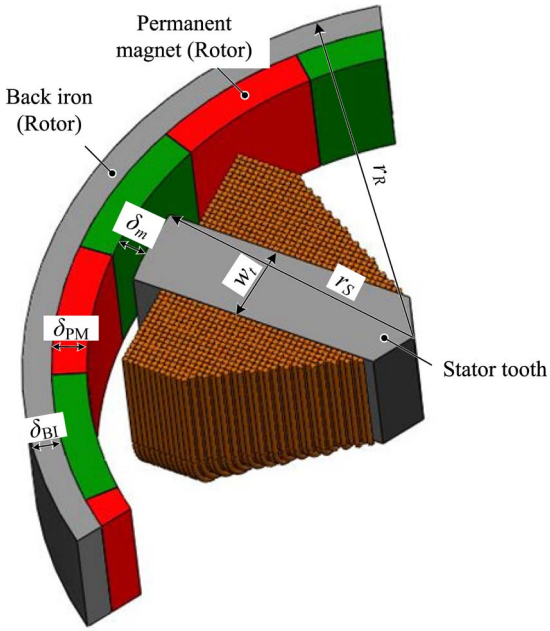

Fig. 8. Design parameters of the motor. The stator teeth are bar shaped according to [30].

Moreover, magnetic saturation in the stator teeth needs to be considered for this optimization step.

The optimal values found for the proposed 300-W motor are presented in Table I. The rated torque of 6 Nm is achievable when the maximum current according to (12) is applied. The maximum producible torque for this motor is 12 Nm. However, very high drive currents are needed, and the maximum current density is clearly exceeded. Therefore, only very short torque peaks are practicable.

VI. Thermal Analysis

To analyze the thermal properties of the motor, the occurring losses need to be determined. Both eddy current and hysteresis losses are generated in the stator and rotor parts due to changing magnetic fields. Additionally, there will be ohmic losses in the stator windings. The losses in the controller will not be considered in this paper because they do not lead to a thermal influence in the mixing process.

A. Stator Losses

Since the stator is affected by changing magnetic fields due to the revolving rotor and alternating coil currents, the

TABLE I
RATED VALUES, OPTIMAL DESIGN PARAMETERS, AND CHARACTERISTIC FACTORS OF THE NOVEL BEARINGLESS STIRRER MOTOR

Parameter	Symbol	Value
Stator slot number	q	6
Pole number	$2p$	16
Outer rotor diameter	d_R	148 mm
Magnetic gap thickness	δ_m	5 mm
Maximum current density	$J_{\max}$	5 A/mm^2
Number of windings	N_{coil}	300
Inner rotor diameter	d_{Ri}	126 mm
Magnet thickness	δ_{PM}	6 mm
Back iron thickness	δ_{BI}	5 mm
Stator tooth width	w_t	15 mm
Rated torque	T	6 Nm
Rated angular velocity	ω	50 rad/s
Rated speed	n	~ 500 rpm
Rated drive current	$I_{\text{drv, rms}}$	4.2 A
Radial force current factor	$k_{I,\text{Fr}}$	20 mN/At
Tangential force current factor	$k_{I,\text{Ft}}$	15 mN/At
Total force current factor	$k_{I,F}$	53 mN/At
Radial force displacement factor	k_r	45 N/mm
Axial force displacement factor	k_z	3.2 N/mm
Torque current factor	$k_{I,T}$	3.4

iron material periodically changes its magnetization direction, which leads to hysteresis losses P_{Hys}. These losses can be calculated using

$$P_{\text{Hys}} = c_{\text{Fe,Hys}} \cdot f \cdot p \cdot \hat{B}^{1.6} \cdot m_S \tag{26}$$

where $c_{\text{Fe,Hys}}$ is a material constant, f is the rotational frequency, p is the pole pair number, $\widehat{B}$ is the amplitude of the flux density, and m_S is the stator weight [32].

Moreover, eddy currents are induced in the stator because of the electrical conductivity of the stator iron. This leads to eddy current losses P_{EdC}, which can drastically be reduced by laminating the stator iron, using a stack of thin iron sheets that are isolated against each other. The losses can be determined using

$$P_{\text{EdC}} = c_{\text{Fe,EdC}} \cdot (f \cdot p)^2 \cdot \hat{B}^2 \cdot d_{\text{Fe}}^2 \cdot m_S \tag{27}$$

with the iron sheet thickness d_{Fe} and with another material constant $c_{\text{Fe,EdC}}$ that depends on the mass density and the specific electric reluctance of the stator [32].

In Fig. 9, the occurring losses due to these two effects are plotted dependent on the angular velocity. Even for rated speed, they are in a considerably low range.

B. Rotor Losses

Eddy current losses can arise in the rotor due to the change of the flux density while rotating around the slotted stator. However, 3D-FEM simulations revealed that this change is in a low range (smaller than 0.3 T) and that significant eddy current losses would only appear in the back iron. The alternating magnetic field produced with the stator coils is synchronous

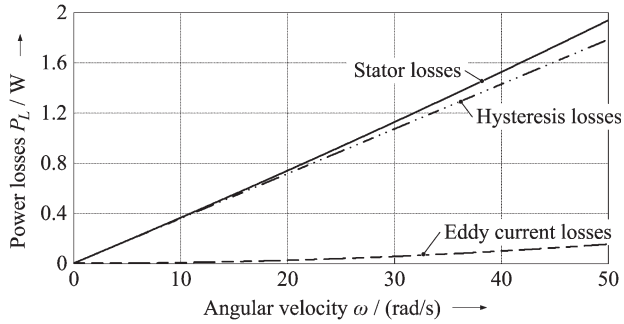

Fig. 9. Stator losses (for rated torque) as the sum of eddy current and hysteresis losses dependent on the angular velocity. The material constants are $c_{\text{Fe,Hys}} = 46$ mW/(Hz T$^{1.6}$ kg) and $c_{\text{Fe,EdC}} = 0.27$ kW/(Hz^2 T^2 m^2 kg), the amplitude of the flux density was found to be 0.8 T for rated torque, and the rotor weight is 0.87 kg.

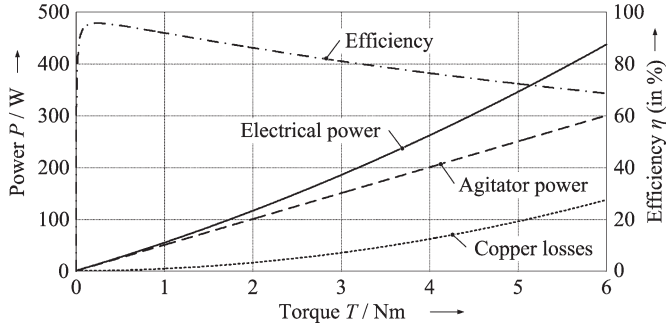

Fig. 10. Electrical power, which is distributed into agitator power (mechanical power) and copper losses (with $R_{\text{Cu}} = 1.24\ \Omega$ per coil), is plotted dependent on the torque for rated speed. The efficiency is lowered with increasing torque. Stator and iron losses have been neglected, whereas a linear function has been chosen for the bearing currents.

with the rotor speed so that no (or only a very low) field change is seen from the rotor. To keep the losses low, the back iron ring should be laminated as well.

C. Copper Losses

The ohmic copper losses P_{Cu} are the largest source for motor losses. They depend on the coil resistance and on the currents through them. Owing to the setup with combined windings (drive and bearing currents superimposed), the calculation becomes

$$P_{\text{Cu}} = 6 \cdot R_{\text{Cu}} \cdot (2n^2 - 2n + 1) \cdot (I_{\text{drv,rms}} + I_{\text{bng,rms}})^2 \tag{28}$$

with the coil resistance R_{Cu} and the rms value of the drive current $I_{\text{drv,rms}}$ and of the bearing current $I_{\text{bng,rms}}$. The factor n describes the ratio between the drive and bearing currents according to (18).

Fig. 10 shows the copper losses in comparison with the agitator power (mechanical power P_{rot}) dependent on the torque at rated speed. The controller has to deliver electrical power P_{elec} to cover both the copper losses and the agitator power. The efficiency η is then given by

$$\eta = \frac{P_{\text{rot}}}{P_{\text{rot}} + P_{\text{Cu}}} = \frac{P_{\text{rot}}}{P_{\text{elec}}}. \tag{29}$$

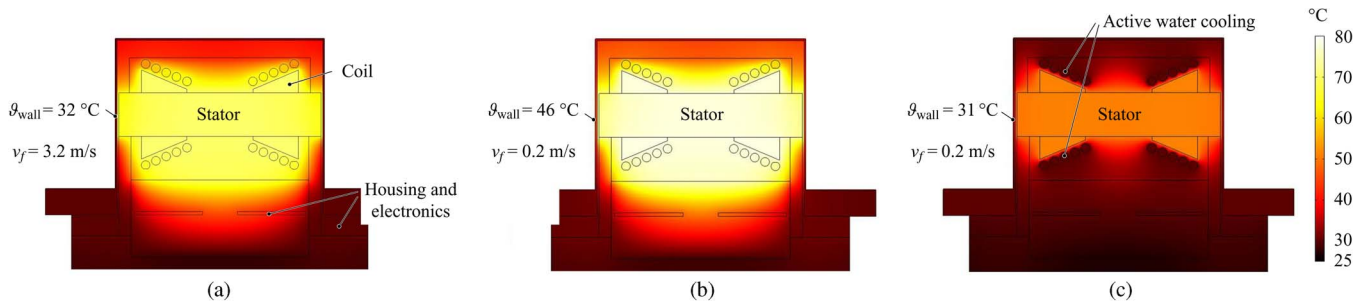

Fig. 11. Thermal simulation of the motor for steady-state operation at rated torque. The occurring losses (135 W) are distributed equally to the coils. The ambient temperature is 25 °C, and the fluid temperature is 30 °C. For high speeds, (a) the wall gets cooled by the process liquid. In case of natural convection only, (b) the wall gets heated critically and (c) unless additional water cooling between the coils is applied.

The influence of both stator and rotor losses has been neglected since they are significantly low. The actual power consumption of the bearing depends on the application, because different flow patterns create different radial forces onto the rotor. Since the bearing does not add to the torque output, any additional power consumption enlarges the losses and, consequently, lowers the efficiency. In Fig. 10, an exemplary bearing current, which was experimentally identified, is used, and it follows the equation

$$i_{\mathrm{bng,rms}} = 215\ \mathrm{mA} + 0.1 \cdot i_{\mathrm{drv,rms}}. \tag{30}$$

D. Thermal Simulations

Reactions in bioreactors are generally very sensitive to heating. For this reason, the temperature of the biological solution is normally regulated during operation. If the rotor is only levitated, no significant losses appear in the motor that could endanger the process. During mixing, however, the losses could become a problem for the reaction when they lead to a local heating of the process liquid. However, since the losses usually appear at higher mixing speeds, the reactor can cope with them (to a certain amount), because larger mixing speed leads to better heat distribution into the whole tank, and then it can be handled by the temperature control.

A bigger problem could arise due to hot reactor walls (where the stator is in direct contact) or due to hot rotor walls. In cell growing reactions, these hot walls could lead to the sterilization of cells passing close to the walls. In Fig. 11, a thermal simulation of the motor and the reactor wall is shown. The ambient temperature is 25 °C, whereas the fluid temperature is 30 °C, which is realistic for a bioreactor process. A constant loss of 135 W (which is observed at rated torque) is distributed to the six coils. It was observed that the reactor wall gets heated only slightly beyond 30 °C (thus, not critical) in case of fluid velocities exceeding 1.6 m/s, which is equivalent to a motor speed of 250 r/min. In Fig. 11(a), no heating of the reactor wall can be observed, because the process liquid has a high velocity of 3.2 m/s (equivalent to rated rotor speed). In this case, the process liquid helps to cool the wall.

Consequently, the most problematic applications in terms of temperature are with high torque at very low speeds. In Fig. 11(b), only natural convection (which is equivalent to a fluid velocity in the range of 0.2 m/s) is cooling the reactor wall, which reaches up to 46 °C in this case. Therefore, additional water cooling, placed on top and/or below the coils, can help to keep the reactor wall temperature low even for very low speeds [cf. Fig. 11(c)].

For the rotor walls, no additional cooling is possible; thus, the losses have to be minimized using constructional measures such as a laminated back iron ring. With this measure, the losses are kept in the range of 100 mW only.

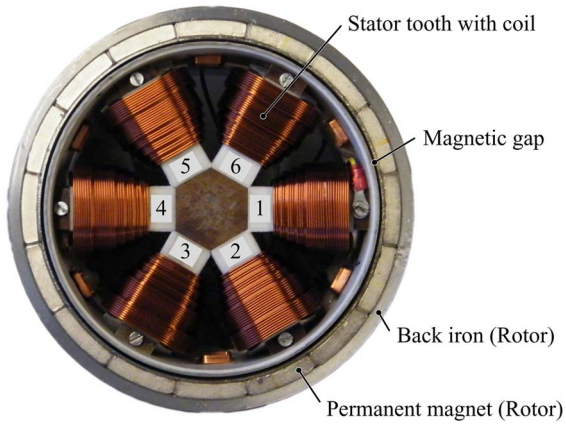

Fig. 12. Top view of the real-size prototype of the novel stirrer motor (without impeller).

VII. Verification With Prototype Setup

A real-size prototype has been built to verify the proper functioning of the motor and to evaluate its performance. In Fig. 12, the bearingless motor is shown during levitation. The combined concentrated coils have to be wound in a cuneiform shape so that the largest possible copper volume can be filled into the available stator slot space.

The results of two practical tests are presented in Fig. 13, showing the measurements of the currents of two opposing coils and of the radial position signals. The bearing and drive currents can be calculated from the two measured currents of coils 1 and 4 by mathematical superposition (addition to get drive and subtraction to get bearing currents). In Fig. 13(a), a test mixing application is shown, where a prototype impeller (mounted onto the rotor) stirs inside a 60-L water tank with 6 Nm at 280 r/min, whereas in Fig. 13(b), the rotor is operated in air with 500 r/min. In the middle column, a steady-state operation is shown. It can

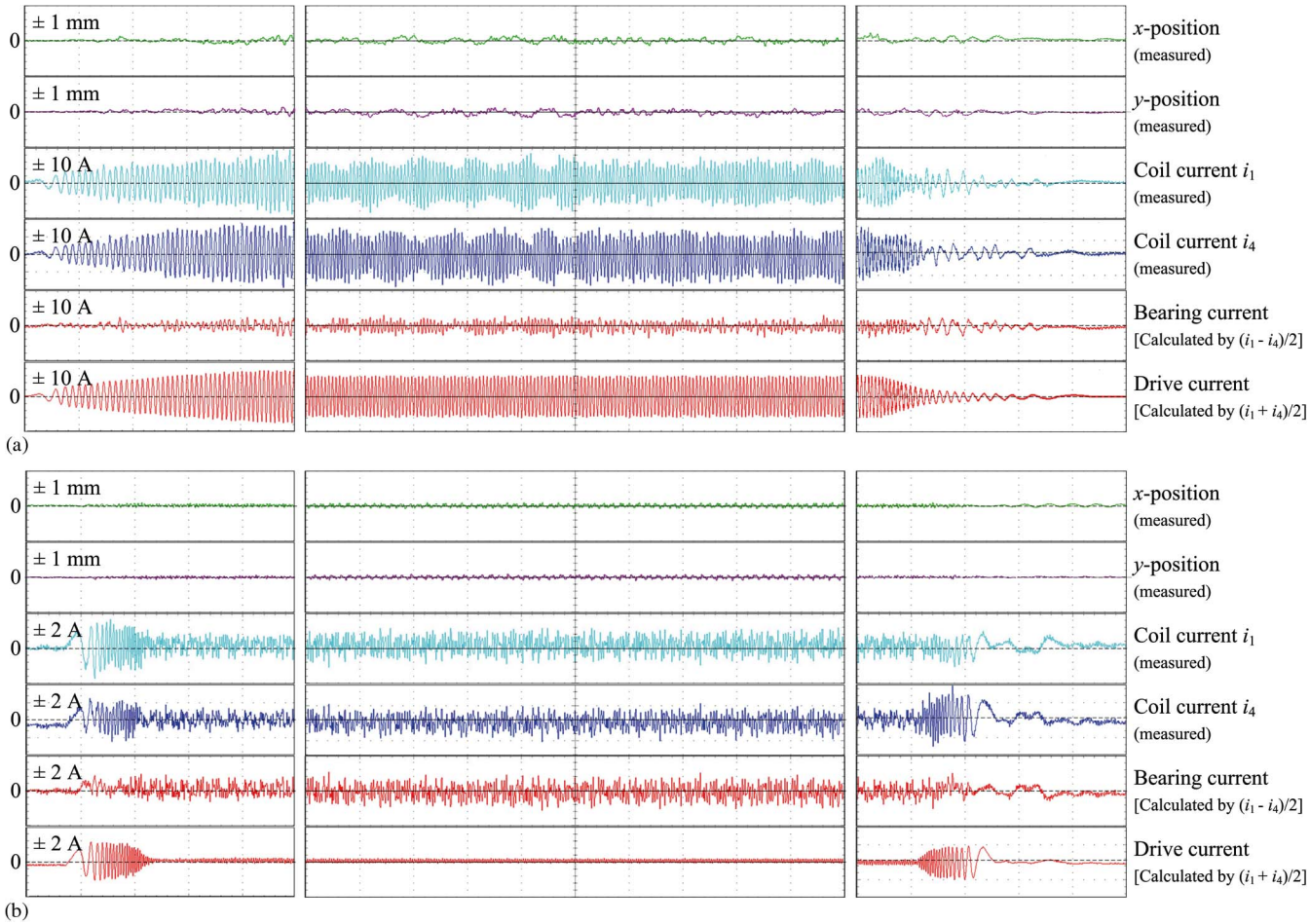

Fig. 13. Measurements of the currents of two opposite coils and of the radial positions during operation (a) in a test water tank of 60 L and (b) in air. The middle column shows the steady-state operation (a) at rated torque (6 Nm) with a rotational speed of 280 r/min or (b) without load torque at 500 r/min. The radial displacement during the whole operation in water is smaller than 200 μm, which is less than 10% movement considering the whole mechanical fluid gap, and this displacement gets even smaller than 100 μm (5%) if operated in air. The bearing as well as the drive current can be calculated from the two measured coil currents. In water (a), the drive current is dominant, whereas it is close to zero in air. The left and right columns show start-up and slow-down behavior, respectively. (Current scale: (a) 10 A/div. and (b) 2 A/div., position scales: 1 mm/div., time scale: 400 ms/div.)

be seen that the radial position is never displaced more than 200 μm from its center position, which is acceptable considering a mechanical fluid gap of 2 mm, and low bearing current is needed to keep the rotor in this working range. (a) The drive current is dominant in the water tank operation, (b) whereas it is close to zero in air since there is no torque load. In the left column, the rotor is accelerated. During this short phase, a high drive current can be measured in (b), which is lower again once the final rotation speed is reached. In the right column, the rotor is actively decelerated.

In Fig. 14, the rotor is actively displaced from its center position into the positive x-direction for 500 μm. It can be seen that in both (a) water and (b) air, a fast position displacement can be achieved. In the water tank, the surrounding fluid damps the rotor displacement and shortens the settling time. Moreover, Fig. 14 reveals that the two radial axes can be controlled independently and do not influence each other.

In Fig. 15, the rotor position in the axial direction during rotation in air is shown. In a first step, the rotor is pushed down for 2 mm and later released so that it jumps back to its working position. The axial damping in air is small; thus, the oscillations cease only slowly. This situation is highly improved once the rotor is operated in water. In that case, the oscillations cease within half of the time when only the rotor without mixer head is used. Despite these remaining oscillations, the motor can provide the same torque and radial bearing forces because the allowed working range is within a certain axial displacement.

Moreover, additional axial damping can be added to the system with an apt mixer head design. It can be seen in Fig. 15 that a mixer head with a vertical impeller design already dampens the oscillations significantly. If additional horizontal elements are added to the impeller, then the oscillations vanish completely.

VIII. Conclusion

An exterior rotor bearingless brushless motor has been developed, analyzed, optimized, and successfully tested with a real-size prototype in a test tank. It was shown that the control is feasible with combined windings that generate both torque and bearing forces, which leads to an optimized power balance. A thermal analysis revealed that the motor losses are in an acceptable range for rated operation values so that there is no negative impact on the bioreactor application. This novel motor

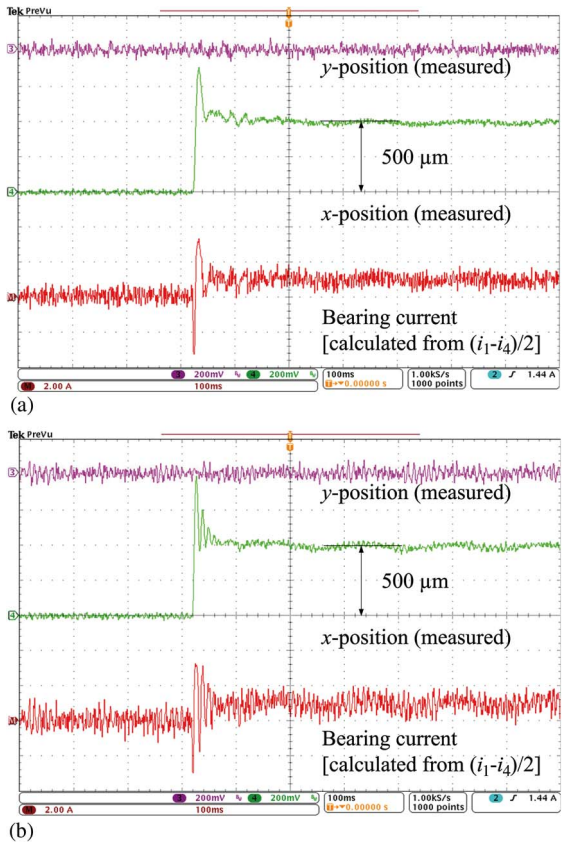

Fig. 14. Measurements of the radial positions and of the bearing current (calculated from the current of two opposed coils). A radial displacement step of 500 μm is performed. The active magnetic bearing can quickly reach the new position in both (a) water and (b) air. However, there is additional damping in the (a) water due to the fluid so that the settling time becomes shorter. (Current scale: 2 A/div., position scales: 250 μm/div., time scale: 100 ms/div.)

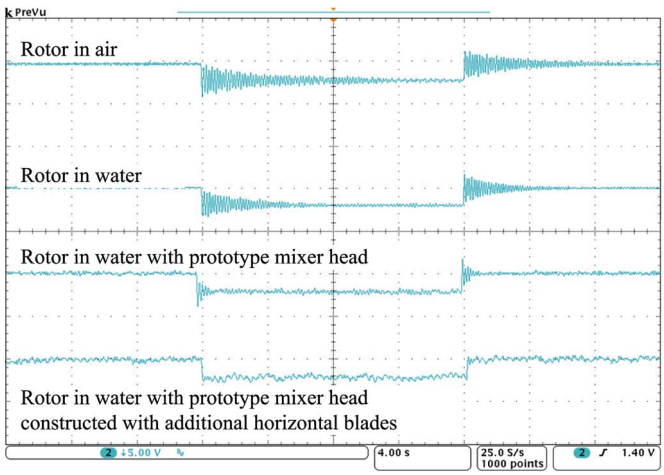

Fig. 15. Measurement of the axial position of the rotor in air and in water. The rotor is pushed down for 2 mm and starts oscillating with a very small damping factor in case of operation in air, since there is no active magnetic bearing in the axial direction. Once the rotor jumps back into its preferred position, the oscillations restart and only vanish after around 8 s. The situation can be improved by running the rotor in water (second measurement), in which case the oscillations vanish twice as fast. With an apt impeller design, the oscillations can be completely damped. (Position scale: 5 mm/div., time scale: 4 s/div.)

is a promising candidate to replace current stirring systems in bioreactors, where it can help to reduce the impact on cell destruction and improve the reaction output.

REFERENCES

[1] D. Mazzei, F. Vozzi, A. Cisternino, G. Vozzi, and A. Ahluwalia, "A high-throughput bioreactor system for simulating physiological environments," *IEEE Trans. Ind. Electron.*, vol. 55, no. 9, pp. 3273–3280, Sep. 2008.

[2] S. S. Ozturk and W.-S. Hu, *Cell Culture Technology for Pharmaceutical and Cell-Based Therapies*. Boca Raton, FL: Taylor & Francis, 2006.

[3] J. A. Asenjo and J. C. Merchuk, *Bioreactor System Design*. New York: Marcel Dekker, 1995.

[4] K. van't Riet and J. Tramper, *Basic Bioreactor Design*. New York: Marcel Dekker, 1991.

[5] S. Ye and K. T. Chau, "Chaoization of DC motors for industrial mixing," *IEEE Trans. Ind. Electron.*, vol. 54, no. 4, pp. 2024–2032, Aug. 2007.

[6] R. Schoeb and N. Barletta, "Principle and application of a bearingless slice motor," *JSME Int. J. Ser. C*, vol. 40, no. 4, pp. 593–598, 1997.

[7] W. Amrhein, S. Silber, K. Nenninger, G. Trauner, M. Reisinger, and R. Schoeb, "Developments on bearingless drive technology," *JSME Int. J. Ser. C*, vol. 46, no. 2, pp. 343–348, Jun. 2003.

[8] M. Ooshima, A. Chiba, T. Fukao, and M. A. Rahman, "Design and analysis of permanent magnet-type bearingless motors," *IEEE Trans. Ind. Electron.*, vol. 43, no. 2, pp. 292–299, Apr. 1996.

[9] Y. Christi and M. Moo-Young, "Clean-in-place systems for industrial bioreactors: Design, validation and operation," *J. Ind. Microbiol. Biotechnol.*, vol. 13, no. 4, pp. 201–207, Jul. 1994.

[10] R. Schoeb, "Centrifugal pump without bearings and seals," *World Pumps*, vol. 2002, no. 430, pp. 34–37, Jul. 2002.

[11] A. Chiba, D. Akamatsu, T. Fukao, and M. A. Rahman, "An improved rotor resistance identification method for magnetic field regulation in bearingless induction motor drives," *IEEE Trans. Ind. Electron.*, vol. 55, no. 2, pp. 852–860, Feb. 2008.

[12] K. Raggl, B. Warberger, T. Nussbaumer, S. Burger, and J. W. Kolar, "Robust angle-sensorless control of a PMSM bearingless pump," *IEEE Trans. Ind. Electron.*, vol. 56, no. 6, pp. 2076–2085, Jun. 2009.

[13] T. Tera, Y. Yamauchi, A. Chiba, T. Fukao, and M. A. Rahman, "Performance of bearingless and sensorless induction motor drive based on mutual inductances and rotor displacements estimation," *IEEE Trans. Ind. Electron.*, vol. 53, no. 1, pp. 187–194, Feb. 2006.

[14] W. Gruber, T. Nussbaumer, H. Grabner, and W. Amrhein, "Wide air gap and large-scale bearingless segment motor with six stator elements," *IEEE Trans. Magn.*, vol. 46, no. 6, pp. 2438–2441, Jun. 2010.

[15] F. Zürcher, T. Nussbaumer, W. Gruber, and J. W. Kolar, "Design and development of a 26-pole and 24-slot bearingless motor," *IEEE Trans. Magn.*, vol. 45, no. 10, pp. 4594–4597, Oct. 2009.

[16] S.-M. Yang and M.-S. Huang, "Design and implementation of a magnetically levitated single-axis controlled axial blood pump," *IEEE Trans. Ind. Electron.*, vol. 56, no. 6, pp. 2213–2219, Jun. 2009.

[17] Y. Okada, N. Yamashiro, K. Ohmori, T. Masuzawa, T. Yamane, Y. Konishi, and S. Ueno, "Mixed flow artificial heart pump with axial self-bearing motor," *IEEE/ASME Trans. Mechatronics*, vol. 10, no. 6, pp. 658–665, Dec. 2005.

[18] H. Sugimoto, K. Kamiya, R. Nakamura, J. Asama, A. Chiba, and T. Fukao, "Design and basic characteristics of multi-consequent-pole bearingless motor with bi-tooth main poles," *IEEE Trans. Magn.*, vol. 45, no. 6, pp. 2791–2794, Jun. 2009.

[19] S. Zhang and F. L. Luo, "Direct control of radial displacement for bearingless permanent-magnet-type synchronous motors," *IEEE Trans. Ind. Electron.*, vol. 56, no. 2, pp. 542–552, Feb. 2009.

[20] P. Karutz, T. Nussbaumer, W. Gruber, and J. W. Kolar, "Novel magnetically levitated two-level motor," *IEEE/ASME Trans. Mechatronics*, vol. 13, no. 6, pp. 658–668, Dec. 2008.

[21] J. Boehm, R. Gerber, J. R. Hartley, and S. Whitley, "Development of active magnetic bearings for high speed rotors," *IEEE Trans. Magn.*, vol. 26, no. 5, pp. 2544–2546, Sep. 1990.

[22] K. Raggl, T. Nussbaumer, and J. W. Kolar, "Comparison of separated and combined winding concepts for bearingless centrifugal pumps," *J. Power Electron.*, vol. 9, no. 2, pp. 243–258, Mar. 2009.

[23] T. Reichert, T. Nussbaumer, W. Gruber, and J. W. Kolar, "Design of a novel bearingless permanent magnet motor for bioreactor applications," in *Proc. 35th IEEE IECON*, Nov. 2009, pp. 1086–1091.

[24] S. Earnshaw, "On the nature of molecular forces which regulate the constitution of the luminiferous ether," *Trans. Camb. Phil. Soc.*, vol. 7, pp. 97–112, 1842.

[25] T. Schneeberger, T. Nussbaumer, and J. W. Kolar, "Magnetically levitated homopolar hollow-shaft motor," *IEEE/ASME Trans. Mechatronics*, vol. 15, no. 1, pp. 97–107, Feb. 2010.

[26] S. Silber, W. Amrhein, P. Boesch, R. Schoeb, and N. Barletta, "Design aspects of bearingless slice motors," *IEEE/ASME Trans. Mechatronics*, vol. 10, no. 6, pp. 611–617, Dec. 2005.
[27] F. Zürcher, T. Nussbaumer, and J. W. Kolar, "Principles of magnetic levitation and motor torque generation by superposition of harmonics in bearingless brushless motors," in *Proc. 35th IEEE IECON*, Nov. 2009, pp. 1246–1251.
[28] M. T. Bartholet, T. Nussbaumer, D. Krahenbühl, F. Zürcher, and J. W. Kolar, "Modulation concepts for the control of a two-phase bearingless slice motor utilizing three-phase power modules," *IEEE Trans. Ind. Appl.*, vol. 46, no. 2, pp. 831–840, Apr. 2010.
[29] T. Reichert, T. Nussbaumer, and J. W. Kolar, "Novel bearingless brushless motor in exterior rotor construction for stirred bioreactors," in *Proc. 5th IET Int. Conf. PEMD*, Apr. 2010, pp. 1–6.
[30] P. Karutz, T. Nussbaumer, W. Gruber, and J. W. Kolar, "Acceleration-performance optimization for motors with large air gaps," *IEEE Trans. Ind. Electron.*, vol. 57, no. 1, pp. 52–60, Jan. 2010.
[31] P. Karutz, T. Nussbaumer, W. Gruber, and J. W. Kolar, "Saturation effects in high acceleration bearingless slice motors," in *Proc. IEEE Int. Symp. Ind. Electron.*, 2008, pp. 472–477.
[32] C. P. Steinmetz, "On the law of hysteresis," *Proc. IEEE*, vol. 72, no. 2, pp. 196–221, Feb. 1984.

Thomas Reichert (S'09) was born in Schaffhausen, Switzerland, in 1983. He received the M.Sc. degree in electrical engineering and information technology in 2008 from the Swiss Federal Institute of Technology (ETH) Zurich, Zurich, Switzerland, where he is currently working toward the Ph.D. degree.

The focus during his studies was on mechatronics, robotics, power systems, and control. During his master's thesis, he simulated rotor dynamics and implemented a magnetic bearing for a megaspeed drive. Since October 2008, he has been with the Power Electronic Systems (PES) Laboratory, ETH Zurich, where he works on high-torque magnetically levitated motors.

Thomas Nussbaumer (S'02–M'06) was born in Vienna, Austria, in 1975. He received the M.Sc. degree (with honors) in electrical engineering from the University of Technology Vienna, Vienna, in 2001 and the Ph.D. degree from the Swiss Federal Institute of Technology (ETH) Zurich, Zurich, Switzerland, in 2004.

From 2001 to 2006, he has been with PES, where he has done research on modeling, design, and control of three-phase rectifiers, power factor correction techniques, and electromagnetic compatibility. Since 2006, he has been with Levitronix GmbH, Zurich, where he is currently working on bearingless motors, magnetic levitation, and permanent-magnet motor drives for the semiconductor and biotechnology industry. His current research is focused on compact and high-performance mechatronic systems including novel power electronics topologies, control techniques, drive systems, sensor technologies, electromagnetic interference (EMI), and thermal aspects.

Johann W. Kolar (M'89–SM'04–F'10) received the Ph.D. degree (*summa cum laude/promotio sub auspiciis praesidentis rei publicae*) from the University of Technology Vienna, Vienna, Austria.

Since 1984, he has been an Independent International Consultant in close collaboration with the University of Technology Vienna, in the fields of power electronics, industrial electronics, and high performance drives. He has proposed numerous novel PWM converter topologies and modulation and control concepts, e.g., the VIENNA rectifier and the three-phase ac–ac sparse matrix converter. He has published over 300 scientific papers in international journals and conference proceedings and has filed more than 75 patents. He was appointed Professor and Head of the Power Electronic Systems Laboratory at the Swiss Federal Institute of Technology (ETH) Zurich, Zurich, Switzerland, on February 1, 2001. The focus of his current research is on ac–ac and ac–dc converter topologies with low effects on the mains, e.g., for power supply of telecommunication systems, more-electric-aircraft and distributed power systems in connection with fuel cells. Further main areas are the realization of ultracompact intelligent converter modules employing the latest power semiconductor technology (SiC), novel concepts for cooling and EMI filtering, multidomain/multiscale modeling and simulation, pulsed power, bearingless motors, and power MEMS.

Dr. Kolar is a member of the IEEJ and the technical program committees of numerous international conferences in the field (e.g., Director of the Power Quality Branch of the International Conference on Power Conversion and Intelligent Motion). From 1997 to 2000, he has been serving as an Associate Editor of the IEEE TRANSACTIONS ON INDUSTRIAL ELECTRONICS and since 2001 as an Associate Editor of the IEEE TRANSACTIONS ON POWER ELECTRONICS. Since 2002, he has also been an Associate Editor of the *Journal of Power Electronics* of the Korean Institute of Power Electronics and a member of the Editorial Advisory Board of the IEEJ Transactions on Electrical and Electronic Engineering. He received the Best Transactions Paper Award from the IEEE Industrial Electronics Society in 2005. He also received an Erskine Fellowship from the University of Canterbury, New Zealand, in 2003. In 2006, the European Power Supplies Manufacturers Association (EPSMA) awarded the Power Electronics Systems Laboratory of ETH Zurich as the leading academic research institution in Europe.